Supercell Case on a Reduced Radius Sphere

Joe Klemp, Bill Skamarock, and Sang-Hun Park, NCAR

27 May 2014

Atmospheric sounding

For the supercell test case, we initialize the atmosphere with an idealized thermodynamic sounding that has large CAPE ($\sim$ 2200 m^{2}s^{-2}). Following Weisman et al. (1982, 1984, 1987), we specify the potential temperature profile $\bar{\theta}(z)$ as

$$\bar{\theta}(z) = \begin{cases} \theta_0 + (\theta_{tr} - \theta_0)\left(\dfrac{z}{z_{tr}}\right)^{\frac{5}{4}}, & \text{for } z \le z_{tr} \ ; \\ \theta_{tr} \exp\left[\dfrac{g}{c_p T_{tr}}(z - z_{tr})\right], & \text{for } z > z_{tr} \ , \end{cases} \tag{1}$$

where θ_0 is the surface potential temperature, and $\theta_{tr} = 343$ K represents the potential temperature at the tropopause at $z_{tr} = 12$ km. The stratosphere is isothermal at $T_{tr} = 213$ K. The relative humidity profile $H(z)$ is given by

$$H(z) = \begin{cases} 1 - \dfrac{3}{4}\left(\dfrac{z}{z_{tr}}\right)^{\frac{5}{4}}, & \text{for } z \le z_{tr} \ ; \\ \dfrac{1}{4}, & \text{for } z > z_{tr} \ . \end{cases} \tag{2}$$

The initial water-vapor mixing ratio is defined from $\bar{q}_v(z) = H(z)\bar{q}_{vs}$, where the saturation mixing ratio is taken from Klemp and Wilhelmson (1978, eq. 2.11):

$$\bar{q}_{vs}(z) = \frac{380}{\bar{p}(z)} \exp\left(17.27\frac{T - 273}{T - 36}\right). \tag{3}$$

Here, the initial pressure $\bar{p}(z)$ is expressed in hPa. In addition, the mixing ratio is constrained to a maximum value of $q_{v0} = 14$ g/kg to approximate a well-mixed boundary layer in the lowest kilometer. The temperature and moisture profiles for this sounding are shown in Figure 1. The Convective Available Potential Energy (CAPE) for the sounding is about 2200 m^{2}s^{-2}, which is conducive for supercell formation.

In past idealized supercell simulations, we have used an environmental wind profile characterized by a linear shear below $z_s = 5$ km, with constant winds aloft. However, in balancing the initial state on the sphere, a discontinuity in the wind shear ($\partial\bar{u}/\partial z$) leads to a discontinuity in potential temperature away from the equator. Therefore, we have removed this discontinuity by specifying a polynomial fit for $\bar{u}$ for $z_s - 1000 < z < z_s + 1000$ that matches the value and slope of $\bar{u}$ at $z = z_s \pm 1000$. The mean wind is then scaled by $\cos\phi$ to maintain solid-body rotation at each level on the sphere, yielding:

$$\bar{u}(\phi, z) = \begin{cases} \left[U_s\left(\dfrac{z}{z_s}\right) - U_c\right]\cos\phi & \text{for} \quad z < z_s - 1000 \ ; \\ \left[\left(-\frac{4}{5} + 3\frac{z}{z_s} - \frac{5}{4}\frac{z^2}{z_s^2}\right)U_s - U_c\right]\cos\phi & \text{for } |z - z_s| < 1000 \ ; \\ \left[U_s - U_c\right]\cos\phi & \text{for} \quad z > z_s + 1000 \ . \end{cases} \tag{4}$$

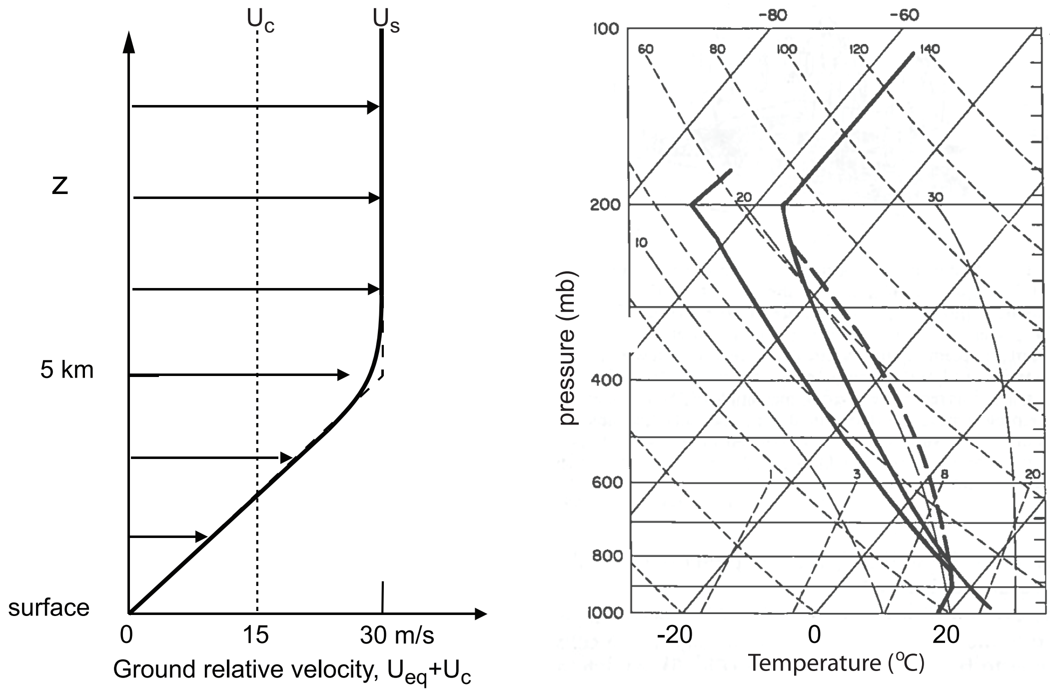

Figure 1. Mean wind and thermodynamic sounding at the equator for the supercell simulation on a reduced radius sphere.

We specify $U_s = 30$ ms^{-1} to provide a strong wind shear that is conducive to supercell storm development, and set a coordinate translation speed $U_c = 15$ ms^{-1} at the equator to render the storm nearly stationary in the model coordinates. Defining $U_{eq} = \bar{u}(0, z)$, the ground relative initial wind at the equator is then $U_{eq} + U_c$ (see Figure 1).

Although there is no Coriolis force in these simulations, the presence of vertical wind shear requires latitudinal variation of the potential temperature and pressure to maintain a balanced state in the absence of imposed perturbations. To achieve this balance, the initial fields must satisfy both the hydrostatic equation:

$$\frac{\partial \pi}{\partial z} = -\frac{g}{c_p \theta_v} \tag{5}$$

and the gradient wind equation:

$$u^2 \tan \phi = -c_p \theta_v \frac{\partial \pi}{\partial \phi}, \tag{6}$$

where θ_v is the virtual potential temperature and π is the Exner function, Cross differentiating these two equations and equating $\pi_{\phi z}$, we obtain the following equation for θ_v:

$$\frac{\partial {\theta_v}^{(i+1)}}{\partial \phi} = \frac{\sin 2\phi}{2g} \left\{ U_{eq}^2 \frac{\partial {\theta_v}^{(i)}}{\partial z} - {\theta_v}^{(i)} \frac{\partial U_{eq}^2}{\partial z} \right\}, \tag{7}$$

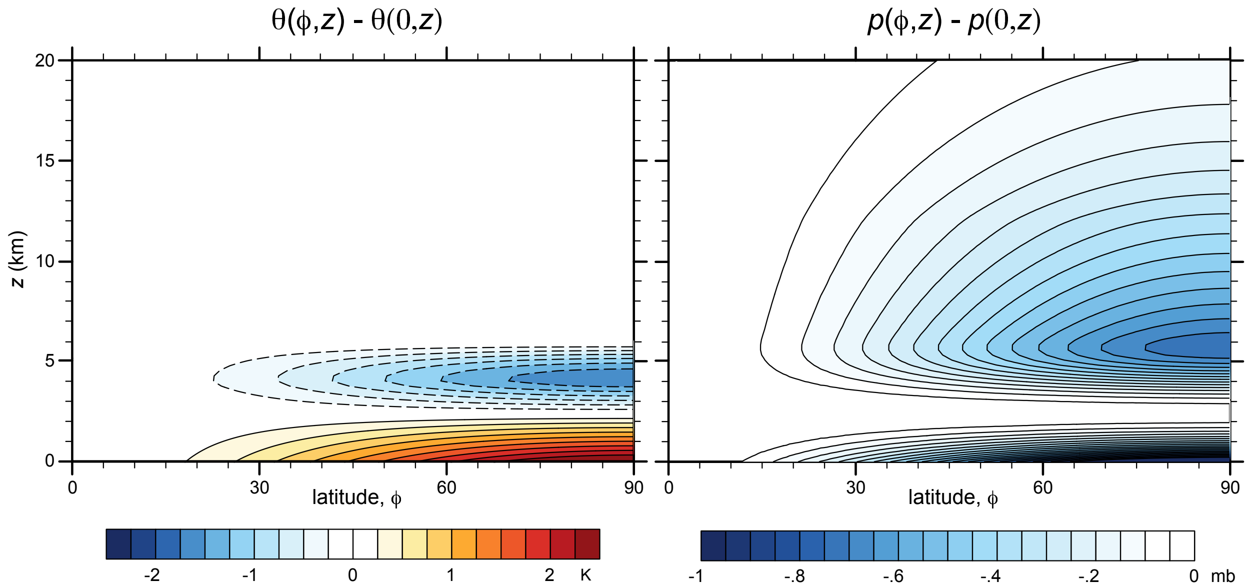

Figure 2. Deviation of potential temperature (K) and pressure (mb) from their values at the equator as a function of latitude

where U_{eq} is the initial zonal wind at the equator. This equation can be readily solved by iteration (as indicated by the i superscripts), and is found to converge in 2-3 iterations. After computing a balanced θ_v from (7), the corresponding balanced pressure is obtained from the hydrostatic equation (5), after adjusting the pressure along the top of the domain using (6). The moisture $\bar{q}_v(z)$ is computed based on the thermodynamic sounding at the equator,and does not vary with latitude. The variations of the balanced initial thermodynamic fields with latitude are displayed in Figure 2. The maximum deviations (about 2.5^o K for θ and -1 mb for p occur at the surface at the poles. Notice that these variations from their values at the equator depend only on latitude, and not on the radius reduction of the sphere.

Model domain configuration

For this supercell test case on a reduced-radius sphere, we specify a radius reduction factor of $X = 120$, which provides a large enough sphere to maintain good quantitative correspondence with comparable simulations on a flat plane (see further discussion in results section). The simulation domain is 20 km in depth, with a uniform vertical grid spacing of $\Delta z = 500$ m and a free-slip boundary condition is imposed along the lower surface. We begin with a nominally uniform horizontal grid spacing of about 500 m, which appears to yield nearly converged solutions with the diffusion specified as outlined below. Coarser horizontal grids may also be considered to evaluate the dependence of simulated storm evolution as a function of horizontal resolution. With the 500 m grid, we integrate MPAS forward in time using a 3 s time step.

Initial thermal perturbation

To initiate convection, a thermal perturbation is introduced in the initial potential temperature field. It is defined according to the expression

$$\theta_i(\lambda, \phi, z) = \begin{cases} \bar{\theta}(\phi, z) + \Delta\theta \cos^2\Big(\dfrac{\pi}{2} R_\theta\Big) & \text{for } R_\theta < 1 \ ; \\ \bar{\theta}(\phi, z) & \text{for } R_\theta \geq 1 \ , \end{cases} \tag{8}$$

where

$$R_\theta = \left[\Big(\frac{r}{r_h}\Big)^2 + \Big(\frac{z - z_c}{r_z}\Big)^2 \right]^{\frac{1}{2}}. \tag{9}$$

Here, $r(\lambda, \phi, \lambda_c, \phi_c)$ is the great circle distance from the center of the thermal perturbation at (λ_c, ϕ_c), and is defined (see DCMIP eq. 77) by

$$r(\lambda, \phi, \lambda_c, \phi_c) = \frac{a_{ref}}{X} \arccos[\sin\phi_c \sin\phi + \cos\phi_c \cos\phi \cos(\lambda - \lambda_c)]. \tag{10}$$

The parameters in (8)-(9) are specified as $\Delta\theta = 3$ K, $r_h = 10$ km, and $z_c = r_z = 1.5$ km.

Cloud microphysics

To represent the cloud microphysical processes, we utilize a simple Kessler parameterization that contains three moisture species: water vapor (q_v), cloud water (q_c), and rain water (q_r). This parameterization (described in Klemp and Wilhelmson, 1978) is called at the end of each time step and updates the potential temperature and moisture variables according to the equations:

$$\frac{\Delta\theta}{\Delta t} = -\frac{L}{c_p \pi}\Big(\frac{\Delta q_{vs}}{\Delta t} + E_r\Big) \tag{11}$$

$$\frac{\Delta q_v}{\Delta t} = \frac{\Delta q_{vs}}{\Delta t} + E_r \tag{12}$$

$$\frac{\Delta q_c}{\Delta t} = -\frac{\Delta q_{vs}}{\Delta t} - A_r - C_r \tag{13}$$

$$\frac{\Delta q_r}{\Delta t} = - E_r + A_r + C_r - V_r \frac{dq_r}{dz}. \tag{14}$$

Here, L is the latent heat of condensation, A_r is the autoconversion rate of cloud water to rain water, C_R is the collection rate of rain water, E_r is the rain water evaporation rate, and V_r is the rain water terminal velocity. For each variable ϕ, $\Delta\phi = \phi^{t+\Delta t} - \phi^*$, where ϕ^* is the value at the new time level prior to the final microphysics update. A listing of the fortran code for this parameterization is contained in the file kessler_z.pdf.

Physical and numerical diffusion

Dissipation is an important component of convective storm simulations. Because the smallest scales tend to be the most unstable, the dominant scales of the evolving convection are strongly influenced by the relative strengths of latent heating and dissipation at the smaller scales. For this test case, we have specified constant-coefficient ($\nu = 500$ m^2/s) second order diffusion terms (both horizontal and vertical) in each of the prognostic equations, with an inverse Prandtl number of 3 for the scalar equations. In the vertical direction, this mixing is applied to the perturbation from the initial mean state to prevent the initial balanced state from being mixed out. Although this is not as realistic as a sub-grid TKE or Smagorinski scheme, using a constant physical viscosity allows the numerical solutions to be converged as the grid is sufficiently refined (which will not occur using TKE or Smagorinsky because of their dependence on the grid scale).

We have also experimented with using fourth order horizontal filters instead of second order diffusion terms. In these tests, we found that it was necessary to retain the second order vertical diffusion as described above in order to avoid accumulating significant noise in the evolving fields. With the fourth order horizontal filters, the storm system evolved somewhat more rapidly and exhibited more smaller scale structure.

Example results

Simulations were integrated over a 2 h time interval. Figure 4 illustrates the evolution of the maximum vertical velocity during the simulations. The rapid rise in w_{max} over the initial 40-50 minutes is associated with the growth of the initial convective cell. As this initial cell splits into two rotating super cells, w_{max} levels off and maintains an amplitude in the range 40-45 m s^{-1}. Figure 5 displays the evolution of the vertical velocity and rain water fields at 5 km at half-hour intervals. Here the latitudinal position of the fields are shown based on a ground relative framework (i.e. the $U_c = 15$ m s^{-1} has been added back into the translation speed of the storm). By 1 h, the initial updraft has split into two distinct updraft cells, which then propagate farther apart over the second hour.

Figure 6 displays these results at 2 h along with the corresponding fields from the simulation on a flat plane with $\Delta \sim 500$ m and the simulation on the $X = 120$ reduced-radius sphere with $\Delta \sim 1000$ m. The structures of vertical velocity and rain water fields for $\Delta \sim 500$ m are quite similar in the flat-plane and reduced-radius sphere simulations, suggesting that for $X = 120$ the artificial curvature effects on the sphere are not very significant. The reduced-radius sphere simulation for $\Delta \sim 1000$ m maintains the overall splitting supercell structure although a number of quantitative differences are evident. The maximum updraft velocity has some higher frequency variation (Figure 4) and by 2 h stronger secondary convection is developing between the two storms.

Figure 7 displays the vertical velocity fields at $z = 2.5$ km at 2 h for these same three simulations, along with the location of the leading edge of the surface cold pool (taken here as the -0.3° potential temperature contour at the lowest at the lowest model half level at $z = 250$ m). At this 2.5 km level the updrafts are clearly aligned above the convergence line that forms along the edge of the surface cold pool. Notice that in the $X = 120$ simulations the cold pool (and the lower level updrafts) extend laterally to slightly higher latitudes in than in the flat plane simulation. We believe that these differences are caused by the differing environmental conditions that the storms encounter as they propagate to higher latitudes. The speed at which the cold pool of air spreads out beneath the storm is governed in part by the

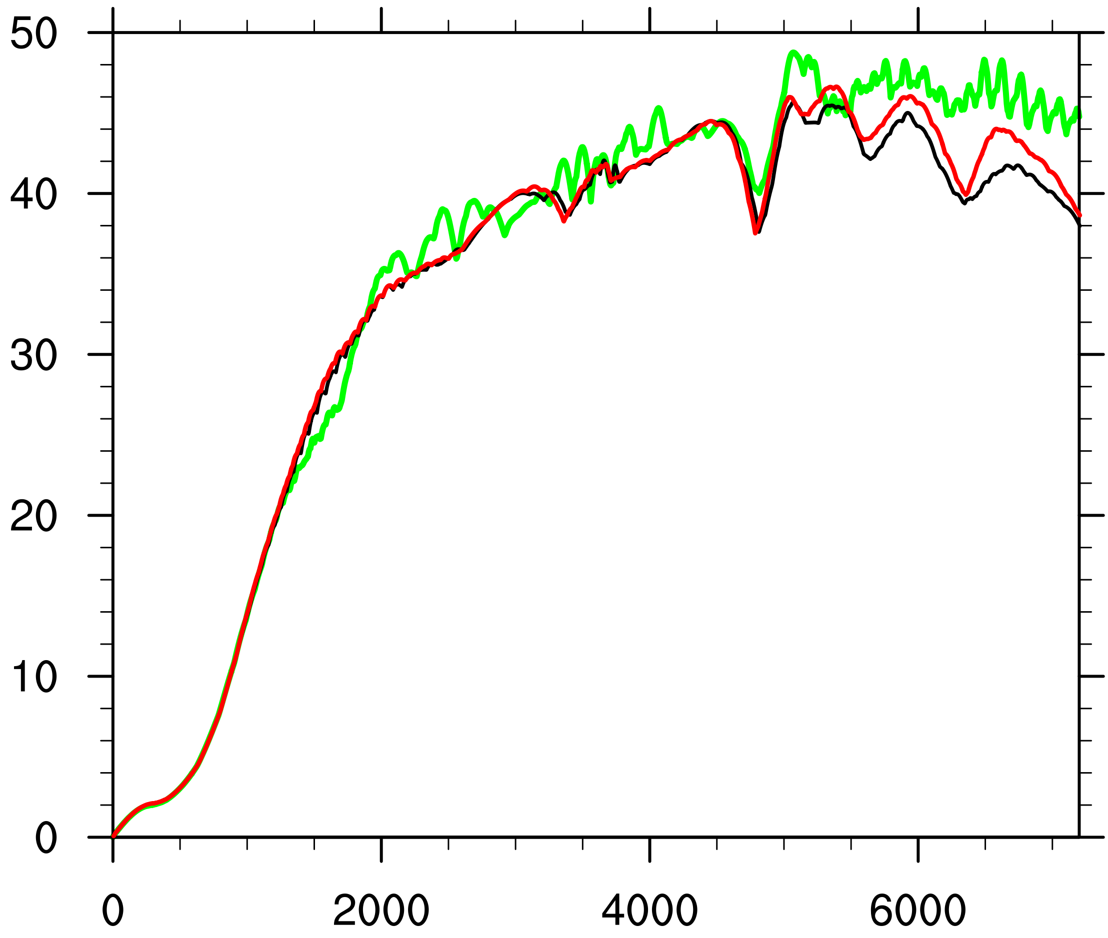

Figure 4. Maximum vertical velocity of supercell updraft for simulation on a flat plane with $\Delta \sim 500$ m (black line), on the reduced-radius sphere with $X = 120$ and $\Delta \sim 500$ m (red line), and on the reduced-radius sphere with $X = 120$ and $\Delta \sim 1000$ m (green line).

temperature difference across the leading edge of the pool (analogous to a gravity current). In the $X = 120$ simulations, the low-level environmental air is somewhat warmer at higher latitudes due to the gradient wind balance imposed on the initial environmental state (see Figure 2). Thus, the cold pool and its associated convergence line in the $X = 120$ simulations propagate laterally a little more rapidly with increasing latitude than in the simulation on a flat plane.

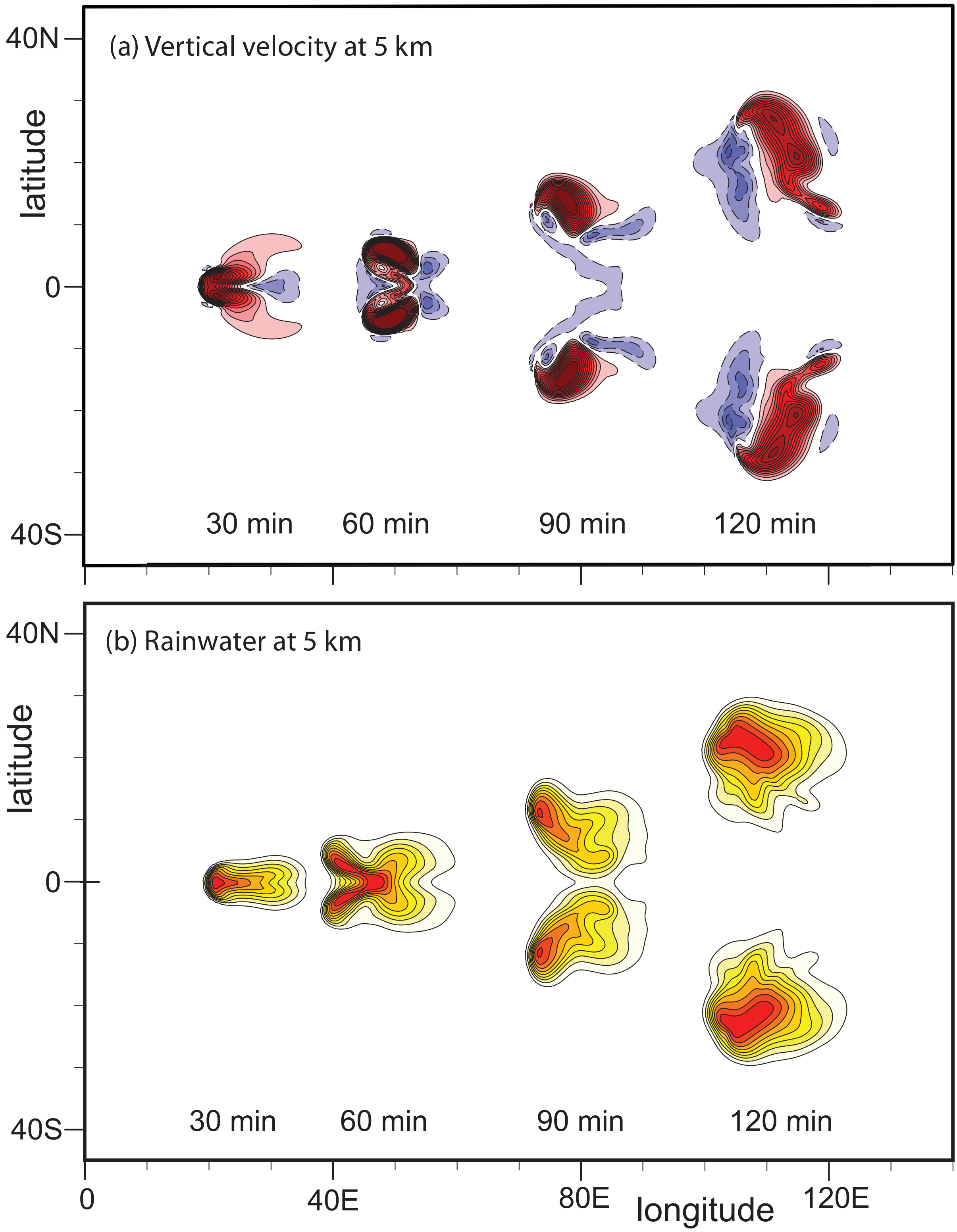

Figure 5. Horizontal cross sections for the simulation with $X = 120$ and $\Delta \sim 500$ m at 5 km at 30 min intervals for (a) vertical velocity (c.i. $= 2$ ms^{-1}) and (b) rain water (c.i $= 1$ gm/kg).

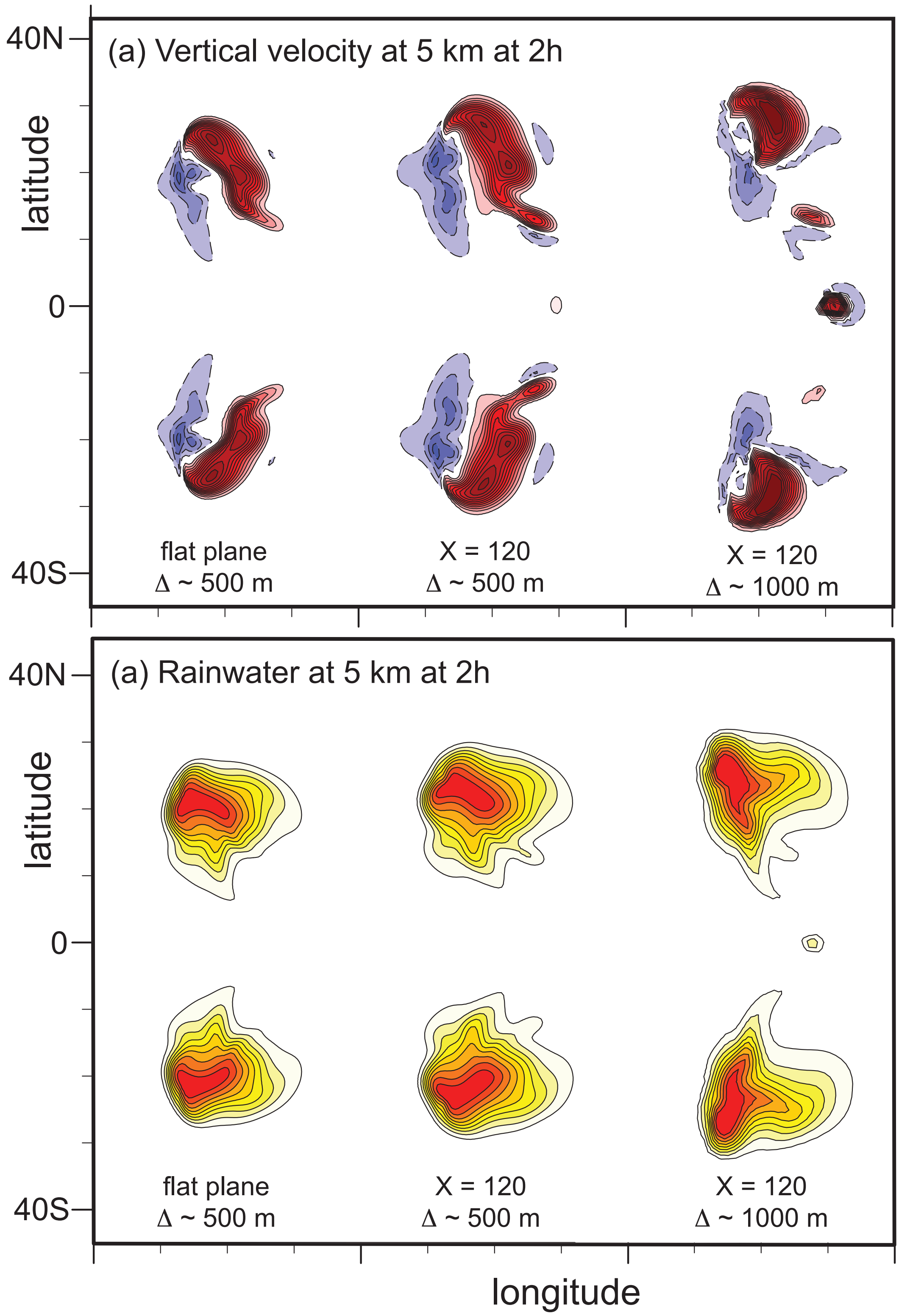

Figure 6. Horizontal cross sections at 5 km at 2 h of (a) vertical velocity (c.i. $= 2$ ms^{-1}), and (b) rain water (c.i $= 1$ gm/kg). Fields are displayed for simulations on a flat plane with $\Delta \sim 500$ m (left), on the reduced-radius sphere with $X = 120$ and $\Delta \sim 500$ m (middle), and on the reduced-radius sphere with $X = 120$ and $\Delta \sim 1000$ m (right).

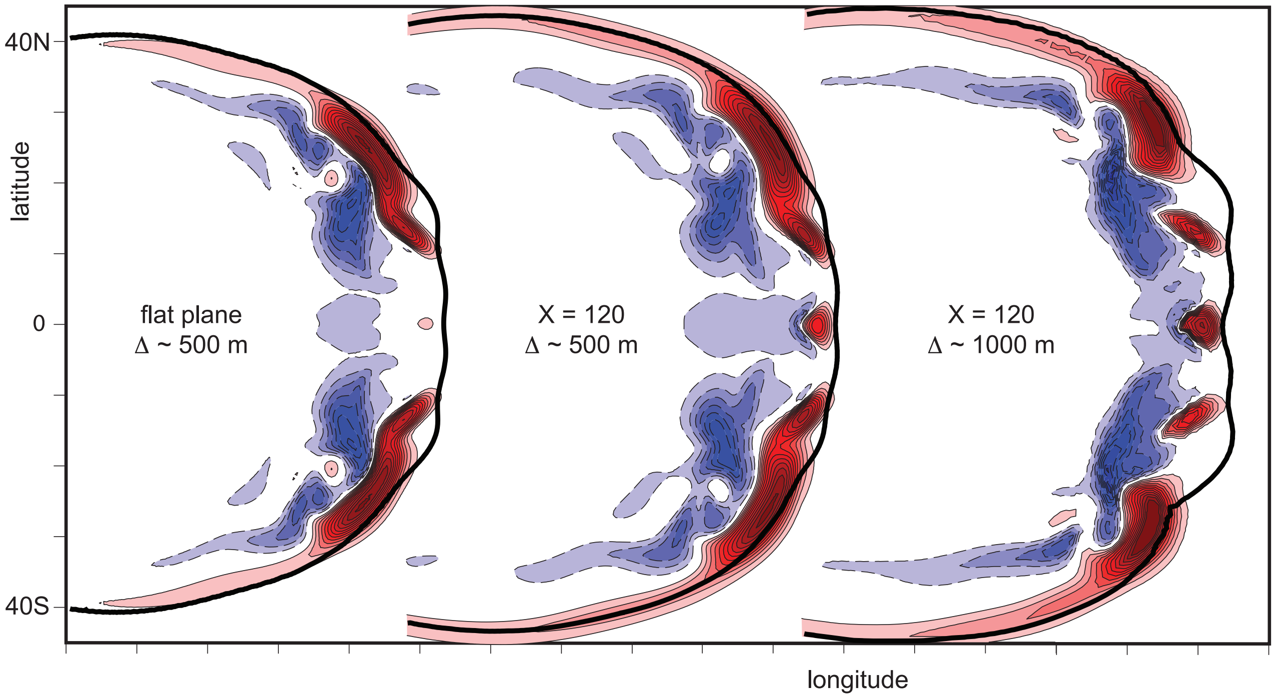

Figure 7. Horizontal cross sections at 2.5 km at 2 h of vertical velocity (c.i. $= 1$ ms^{-1}, displayed for simulations on a flat plane with $\Delta \sim 500$ m (left), on the reduced-radius sphere with $X = 120$ and $\Delta \sim 500$ m (middle), and on the reduced-radius sphere with $X = 120$ and $\Delta \sim 1000$ m (right).The heavy solid line depicts the location of the leading edge of the surface cold pool.

References

Klemp, J. B., and R. B. Wilhelmson, 1978: The simulation of three-dimensional convective storm dynamics. *J. Atmos. Sci.*, **35**, 1070–1096.

Weisman, M. L., and J. B. Klemp, 1982: The dependence of numerically simulated convective storms on vertical wind shear and buoyancy. *Mon. Wea. Rev.*, **110**, 504–520.

Weisman, M. L., and J. B. Klemp, 1984: The structure and classification of numerically simulated convective storms in directionally varying wind shears. *Mon. Wea. Rev.*, **112**, 2479–2498.

Weisman, M. L., J. B. Klemp and R. Rotunno, 1988: The structure and evolution of numerically simulated squall lines. *J. Atmos. Sci.*, **45**, 1990–2013.